1 Version: Revision 1

2 Manuscript number: 6146

3 Accepted date: 2017-3-23

4

5 Electrical conductivity of mudstone before and after dehydration at

6 high temperatures and pressures

7 WENQING SUN[1,2], LIDONG DAI[1,*], HEPING LI[1], HAIYING HU[1,3], LEI WU[1],

8 JIANJUN JIANG[1]

9 *1. Key Laboratory of High-Temperature and High-Pressure Study of the Earth's Interior,*

10 *Institute of Geochemistry, Chinese Academy of Sciences, Guiyang, 550081, China*

11 *2. University of Chinese Academy of Sciences, Beijing, 100049, China*

12 *3. Key Laboratory of Earth and Planetary Physics, Institute of Geology and Geophysics,*

13 *Chinese Academy of Sciences, Beijing, 100029, China*

14

15

16

17

18

19

20

*Corresponding author. Email: dailidong@vip.gyig.ac.cn

1

ABSTRACT

21

22   The electrical conductivity of mudstone before and after dehydration was measured

23   using complex impedance spectroscopy in the frequency range of 10^{-1} to 10^6 Hz, and the

24   experiments were carried out at 0.5–2.5 GPa and 623–973 K. Before and after

25   dehydration, the electrical conductivity of mudstone and temperature followed an

26   Arrhenius relation. The influence of pressure on electrical conductivity was weaker than

27   that of temperature. The conductivity slightly increased with increasing pressure.

28   Dehydration at 760–800 K dramatically enhanced the electrical conductivity of mudstone;

29   the dehydration temperature decreased slightly with increasing pressure.

30   Hydrogen-related lattice defects (e.g., H'_M or $H^\bullet$) are proposed to be the main charge

31   carriers in the mudstone sample before dehydration, whereas H^+ and OH^- are suggested

32   to be the main charge carriers in the dehydration product of mudstone. Finally, the

33   electrical conductivity of the dehydration product of mudstone can be used to interpret

34   high-conductivity layers (HCLs) associated with the Hope and Porters Pass fault zones in

35   Marlborough, New Zealand.

36   **Keywords**: electrical conductivity, mudstone, high pressure, dehydration, conduction

37   mechanism, high-conductivity layer

38

INTRODUCTION

39

40   Electrical conductivity is an important parameter that can be used to infer the

41   material composition and physical conditions of the interior of the Earth and other planets.

42 Previous researchers have studied the electrical conductivities of most minerals and rocks

43 in the Earth's crust and mantle (Huebner and Dillenburg 1995; Dai et al. 2008; Yoshino

44 et al. 2009; Yang et al. 2011; Yang and McCammon 2012; Hu et al. 2013, 2014; Dai and

45 Karato 2014a; Li et al. 2016), and the magnetotelluric (MT) and geomagnetic depth

46 sounding (GDS) results have provided significant constraints (Zhu et al. 2001; Maumus

47 et al. 2005; Yang 2012; Dai et al. 2016; Manthilake et al. 2016). The dehydration of

48 hydrous minerals and rocks (e.g., chlorite, lawsonite, and serpentine) can generate

49 high-conductivity layers (HCLs) in the Earth's interior (Zhu et al. 1999; Manthilake et al.

50 2015, 2016), but the electrical conductivity of pelite containing a large amount of water is

51 unknown.

52   Pelite is widely distributed in the shallow crust, and as the main sedimentary rock

53 that enters subduction zones, it also occurs in the Earth's interior (Li et al. 2005; Song et

54 al. 2015). At high temperatures and high pressures, pelite is metamorphosed, and the

55 dehydration of rock-forming hydrous minerals (e.g., kaolinite, montmorillonite, sericite,

56 and illite) occurs during the subduction of pelite. Song et al. (2009) studied the tectonic

57 evolution of early Palaeozoic high-pressure metamorphic rocks in the North Qilian

58 Mountains of China and obtained peak metamorphic conditions of 2.6 GPa and 813 K for

59 metapelite. Tsuno et al. (2012) suggested that the subduction depths and slab-surface

60 temperatures of pelitic sediments are >100 km and ~1073 K, respectively. The

61 metamorphic grade of pelite differs under various conditions. Some regional

62 metamorphic rocks (e.g., gneiss, schist, and granulite) can form by the metamorphism of

3

63   mudstone, and the electrical properties of natural gneiss and granulite have been studied

64   previously (Fuji-ta et al. 2004, 2007). Li et al. (2005) studied the dehydration temperature

65   of pelite using high-pressure differential thermal analysis (HP-DTA); however, it might

66   be better to determine the dehydration temperature directly using the inflection point

67   between the electrical conductivity and temperature based on the Arrhenius relation

68   (Song et al. 1996; Li et al. 2005).

69   In the present studies, we measured the electrical conductivity of mudstone under *in*

70   *situ* conditions of 0.5–2.5 GPa and 623–973 K. The inflection point of the Arrhenius

71   relation between electrical conductivity and temperature was applied to determine the

72   dehydration temperature of mudstone. The conduction mechanisms before and after the

73   dehydration of mudstone were explored in detail. Furthermore, the results are used to

74   explain HCLs in Marlborough, New Zealand.

75

76   **EXPERIMENTAL PROCEDURES**

77   Sample preparation

78   Fresh mudstone samples were collected from the Tangjiawu Group of the Middle

79   Devonian in Hangzhou, Zhejiang, China. To accurately determine the minerals in the

80   samples, we used optical microscopy, scanning electron microscopy (SEM), and

81   micro-focused X-ray diffraction (XRD) at the State Key Laboratory of Ore Deposit

82   Geochemistry, Institute of Geochemistry, Chinese Academy of Sciences (CAS), Guiyang,

83   China. Based on the statistical volume ratios of all the constituent minerals of mudstone,

84   the main minerals were kaolinite (40%), muscovite (30%), and quartz (20%), and the

85   accessory minerals were hematite (5%) and maghemite (5%).

86   The mudstone samples were ground (<200 mesh) in an agate mortar after being

87   cleaned in a mixture of acetone and ethanol in an ultrasonic cleaning device. The powder

88   was dried at 473 K for 4 h to remove water and then loaded into a copper capsule with a

89   0.025-mm-thick nickel (Ni) foil liner. The height of the capsule was 16 mm, and the inner

90   and outer diameters were 8.0 mm and 8.5 mm, respectively. To avoid the effects of pores

91   and microcracks on the electrical conductivity measurements, the powdered mudstone

92   sample was hot-pressed for 4 h in a multi-anvil high-pressure apparatus at 2.0 GPa and

93   623 K. The hydrothermally annealed samples were cut and polished into cylinders with

94   diameters of 6 mm and heights of 6 mm, and then heated at 473 K for 8 h to eliminate

95   absorbed water for subsequent *in situ* electrical conductivity measurements.

96

97   Impedance measurements

98   The *in situ* electrical conductivity measurements of the mudstone samples were

99   performed   using   the   YJ-3000t   multi-anvil   apparatus   and   a   Solartron-1260

100   Impedance/Gain-phase analyzer at the Key Laboratory of High-Temperature and

101   High-Pressure Study of the Earth's Interior, Institute of Geochemistry, Chinese Academy

102   of Sciences, Guiyang, China. To avoid the influence of absorbed water on the electrical

103   conductivity   measurements,   all   the   components   of   the   experimental   assemblage

104   (pyrophyllite, ceramic tubes and Al_2O_3 and MgO sleeves) were heated at 1073 K for 8 h

105   in a muffle furnace. Fig. 1 shows the sample assembly for the electrical conductivity

106   measurements. Pyrophyllite cubes ($32.5 \times 32.5 \times 32.5$ mm^3) and three-layer stainless

107   steel sheets (total thickness of 0.5 mm) were used as the pressure media and heater,

108   respectively. A layer of nickel foil (thickness of 0.025 mm) was placed between the

109   alumina and magnesia sleeves to shield against external electromagnetic and spurious

110   signal interference. The alumina and magnesia sleeves were insulating and transmitted

111   pressure well. The sample was loaded into the magnesia tube. The parallel-plate electrode

112   was composed of two nickel disks (6.0 mm in diameter and 0.5 mm in thickness) on the

113   tops and bottoms of the samples. Temperatures with errors of ±5 K were measured using

114   a NiCr–NiAl thermocouple. The pressure error was ±0.1 GPa.

115   The impedance spectra of the mudstone samples were collected at 0.5–2.5 GPa and

116   623–973 K. A Solartron-1260 Impedance/Gain-phase analyzer with an applied voltage of

117   1 V and frequency range of 10^{-1}–10^6 Hz was used to collect impedance spectra of

118   samples when the desired pressure and temperature were stable. The pressure was slowly

119   increased to the desired value (1.0 GPa/h) and was then increased at a rate of 100 K/h.

120   The impedance spectra were measured at certain temperatures, which were changed at

121   50-K intervals. Each mudstone sample was maintained at each temperature for 30 min,

122   and the impedance spectra were obtained. To clearly display the variations in the

123   electrical conductivities of the mudstone samples during dehydration, the impedance

124   spectra were continuously collected for ~500 min at 2.5 GPa and 823 K. The electrical

125   conductivity measurements on the mudstone samples were performed in two heating and

126   cooling cycles at 1.5 GPa to confirm the reproducibility of the conductivity results.

127

RESULTS

128

129   Representative complex impedance spectra of the mudstone samples at 2.5 GPa are

130   shown in Fig. 2. All the impedance spectra at the different temperatures contained almost

131   ideal semicircles in the high-frequency domain and additional tails in the low-frequency

132   domain. The ideal semicircles represent the bulk electrical properties of the sample, and

133   the additional tails are the typical characteristic of the sample–electrode interface in

134   diffusion processes (Roberts and Tyburczy 1991; Dai et al. 2014; Hu et al. 2015).

135   Therefore, the bulk sample resistance can be determined by fitting the high-frequency arc.

136   The equivalent circuit is composed of the series connection of R_S–CPE_S (R_S and CPE_S

137   represent the resistance and constant-phase element of a sample, respectively) and

138   R_E–CPE_E (R_E and CPE_E represent the interaction of the charge carrier with the electrode).

139   All the fitting errors were less than 5% of the electrical resistance. The electrical

140   conductivities of the samples were calculated as follows:

141
$$\sigma = L / SR \tag{1}$$

142   where L is the height of a sample (m), S is electrode cross-sectional area (m^2), R is fitting

143   resistance (Ω), and σ is sample electrical conductivity (S/m).

144   The logarithmic electrical conductivities of the mudstone samples at pressures of

145   0.5–2.5 GPa and temperatures of 623–973 K are plotted against reciprocal temperature in

146   Fig. 3. The relationship between the electrical conductivities and temperature before and

147   after dehydration fits the Arrhenius equation:

148
$$\sigma = \sigma_0 \exp(-\Delta H / kT) \tag{2}$$

149   where σ_0 is a pre-exponential factor (K·S/m), k is the Boltzmann constant (eV/K), T is the

7

150   absolute temperature (K), and ΔH is the activation enthalpy (eV), which can be expressed

151   with the following thermodynamic equation:

152

$$\Delta H = \Delta U + P \Delta V \tag{3}$$

153   where ΔU, ΔV, and P are the activation energy (eV), activation volume (cm^3/mol), and

154   pressure (GPa), respectively. All the fitting parameters of the bulk sample conductivity

155   are listed in Table 1.

156   The electrical conductivities of the samples increased with increasing pressure, and

157   the effect of pressure on conductivity was weaker than that of temperature (Fig. 3). Based

158   on the inflection point of the relationship between the electrical conductivities and

159   temperatures in the pressure range of 0.5–2.5 GPa, we determined the dehydration

160   temperature at each corresponding pressure. As shown in Fig. 3, dehydration temperature

161   (~760–800 K) decreased with increasing pressure. Two representative heating and

162   cooling cycles at 1.5 GPa are displayed in Fig. 4, which confirm the good reproducibility

163   of the experimental data.

164   The relationship between the electrical conductivities of the mudstone samples and

165   the run time during dehydration is shown in Fig. 5. At 2.5 GPa and 823 K, the electrical

166   conductivities of the samples sharply increased during the first 150 min and gradually

167   reached a steady state after 300 min, which indicates that dehydration was complete. The

168   conductivities increased by approximately one order of magnitude during dehydration;

169   the electrical conductivity was ~0.1 S/m after dehydration at 2.5 GPa. The detailed

170   mineralogical assemblages of the mudstone samples before and after dehydration are

171   listed in Table 2. The mineral associations were accurately determined with an optical

172   microscope, XRD, and SEM. A new mineral phase of metakaolinite was formed by the

173   metamorphism of kaolinite at all experimental pressures. The constitution water was

174   released from the samples during the process of dehydration.

175

176   **DISCUSSION**

177   Comparisons with previous studies

178   Kaolinite and muscovite containing large amounts of water were the main minerals

179   of the mudstone samples. These hydrous minerals, which have good interconnectivity,

180   dominate the electrical conductivity of mudstone. The maximum electrical conductivities

181   were approximately 10^{-3} S/m before dehydration, and dramatically increased during

182   dehydration. This result confirms that dehydration significantly affects the electrical

183   conductivity of hydrous minerals and rocks (Zhu et al. 1999; Fuji-ta et al. 2007;

184   Manthilake et al. 2015, 2016; Hu et al. 2017). Metakaolinite was formed by the

185   metamorphism of kaolinite. The remaining rock-forming minerals remained stable during

186   dehydration. The dehydration temperatures (~760–800 K) of the mudstone samples

187   decreased slightly with increasing pressure. Li et al. (2005) indicated that pelite

188   dehydration temperature, as determined by high-pressure differential thermal analysis

189   (HP-DTA), decreases linearly with increasing pressure. The relationships between

190   dehydration temperature and pressure are therefore similar for mudstone and pelite. The

191   dehydration of kaolinite starts at ~673 K at atmospheric pressure, with an upper

192   temperature limit of ~973 K (Pododa et al. 2014). The dehydration temperature range

193   (~760–800 K) of the mudstone samples is within that of kaolinite, indicating that the

194   dehydration minerals in the mudstone samples were kaolinite. The differences in

195   dehydration temperatures between kaolinite and mudstone might be due to different

196   pressures and structures.

197   Manthilake et al. (2015) studied the electrical conductivity of lawsonite, which is

198   also a hydrous mineral. The electrical conductivity of lawsonite before dehydration was

199   approximately two orders of magnitude lower than that after dehydration (Fig. 6). Guo et

200   al. (2011) studied brucite at 3 GPa and 500–1000 K, and found that dehydration results in

201   increasing electrical conductivity. The electrical conductivity of mudstone is lower than

202   that of lawsonite and higher than that of brucite, both before and after dehydration. The

203   differences in their electrical conductivities might be caused by the different experimental

204   conditions and mineral composition. Although the electrical conductivity of kaolinite has

205   not been studied, phlogopite (a common mica) was investigated by Li et al. (2016). The

206   electrical conductivity of phlogopite is approximate to that of mudstone before

207   dehydration and higher than that of mudstone after dehydration. One relatively high

208   activation energy (~2.0 eV) implies that the main conduction mechanism of hydrous

209   phlogopite is ionic conduction (F^+ and K^+ are charge carriers) (Li et al. 2016). In contrast,

210   the much lower activation energy of mudstone (0.64–0.75 eV) shows that its conduction

211   mechanism cannot be ionic conduction. Thus, the electrical conductivity of phlogopite

212   studied by Li et al. (2016) cannot be used to interpret the electrical properties of

213   mudstone.

214   Mudstone is an important protolith of metamorphic rocks (e.g., slate, schist, gneiss,

215   and granulite) in regional metamorphic belts. The electrical conductivities of the

216   dehydration products of mudstone and metamorphic rocks were thus compared with each

217   other (Fig. 6). Granulite is the main metamorphic rock in the lower crust. Its

218   mineralogical assemblage (feldspar, quartz, pyroxene, and garnet) is markedly different

10

219   from that of the dehydration products of mudstone. The electrical conductivities of the

220   mudstone samples after dehydration at 1.5 GPa were close to that of granulite (Fuji-ta et

221   al. 2004), possibly due to various factors (e.g., mineralogical assemblage, conduction

222   mechanism, structure, and chemical composition). Furthermore, serpentinite is an

223   important rock in subduction zones and orogenic belts. Previous studies indicated that the

224   dehydration of serpentinite can explain the HCL (Robertson et al. 2015). Fig. 6 shows

225   that the electrical conductivity of mudstone is higher than that of serpentinite before and

226   after dehydration. The dehydration temperature of mudstone is slightly lower than that of

227   serpentinite (Zhu et al. 1999; Xie et al. 2002).

228

229   Conduction mechanism

230   At a given pressure, the electrical conductivity and temperature of the mudstone

231   samples satisfied the Arrhenius relation before and after dehydration, implying that a

232   dominant conduction mechanism operated in the mudstone samples and dehydration

233   products, respectively. Based on the fitting parameters of the Arrhenius relation, the

234   activation energies of the charge carriers in the samples before and after dehydration

235   were determined to be 0.64–0.75 and 0.36–0.59 eV, respectively.

236   Hematite (Fe_2O_3) and maghemite (γ-Fe_2O_3) are Fe-bearing minerals that occurred in

237   the mudstone samples before and after dehydration; only ferric iron (Fe^{3+}) is present in

238   the two minerals. Hence, small polaron conduction cannot be the conduction mechanism

239   in the mudstone samples. On the other hand, conduction by diffusion of ions is

240   characterized by high activation energies (>2 eV) and positive activation volumes (i.e.,

241   conductivity decreases with increasing pressure) due to the difficulty in the formation and

11

242   migration of cation vacancies at high pressures (Hu et al. 2015). Therefore, ions cannot

243   be the charge carriers in mudstone, as indicated by the low activation energies and

244   negative activation volumes. Proton conduction is considered to be the dominant

245   mechanism in some Fe-free hydrous minerals and rocks (e.g., Dai and Karato 2014a; Dai

246   et al. 2015; Guo 2016). Yang et al. (2011) explored the electrical conductivity of wet

247   clinopyroxene at 0.6–1.2 GPa and 623–1273 K, and determined that the activation

248   enthalpy for proton conduction is 0.73 eV. Dai and Karato (2014b) investigated the

249   influence of FeO and water content on the electrical conductivity of olivine, and found

250   that the activation enthalpy for proton conduction is ~0.82 eV. Guo and Yoshino (2014)

251   studied the pressure-induced enhancement of proton conduction in brucite, and the

252   activation enthalpies for the conductivity of brucite were 0.56–0.72 eV. The activation

253   enthalpies for the conduction of charge carriers in the mudstone samples (0.64–0.75 eV)

254   were close to the values for the conduction of hydrogen in the clinopyroxene, olivine, and

255   brucite samples. Hydrogen-related defects were therefore suggested to be the main charge

256   carriers in the mudstone sample before dehydration. Furthermore, it is suggested that the

257   interconnected fluid in the samples caused the significant increase in electrical

258   conductivity after dehydration. Manthilake et al. (2015) measured the electrical

259   conductivity of lawsonite before and after dehydration at 7 GPa and 298–1320 K. The

260   activation enthalpy for the electrical conductivity of aqueous fluid was 0.32 eV, which

261   was almost 50% less than in the solid phase (Manthilake et al. 2015). The activation

262   enthalpies for the electrical conductivities of dehydration products of the mudstone

263   samples (0.36–0.59 eV) were slightly higher than that of aqueous fluid. This discrepancy

264   may have been caused by the differences in the mineralogical assemblages and

265   experimental conditions. Hence, the migration of H^+ and OH^- of water molecules is

266   suggested as the conduction mechanism for the dehydration products of mudstone.

267

268   Geophysical implications

269   Materials at the Earth's surface can enter the interior through subduction (Ogawa et

270   al. 1994; You et al. 1996; Hawkesworth et al. 1997; Satoh et al. 1998). Pelite is an

271   important sedimentary rock in terms of subducted lithologies and enters the Earth's

272   interior with oceanic basalt. The basalt changes into serpentinite at high temperatures and

273   pressures, and metapelite forms due to the metamorphism of pelite. Metapelite is

274   abundant in subduction zones (Gao et al. 2013; Huang et al. 2013; Gao and Zeng 2014;

275   Yakymchuk and Brown 2014). Hence, it is possible that a certain amount of metapelite

276   occurs in the deep Earth. Walther et al. (1982) confirmed that 5 wt% H_2O and CO_2 are

277   released by the dehydration of pelite at 0.5 GPa and 773 K. Hence, pelite is a significant

278   water source in subduction zones (Walther et al. 1982; Tsuno and Dasgupta 2012). When

279   a subducting plate is heated and compressed, the rocks on top of the plate undergo

280   regional metamorphism (Wyllie 1982). Continental collision occurs after the termination

281   of subduction and the orogenic belt gradually evolves during that process (Song et al.

282   2015). A large amount of free water from the dehydration of pelite can migrate along

283   faults, and aqueous fluids might contribute to the formation of melts (e.g., granitic melts)

284   and regional metamorphism (e.g., serpentinization). Furthermore, aqueous fluids and

285   melts can lead to HCLs (Hyndman et al. 1993; Gaillard et al. 2008; Ni et al. 2011; Rao et

286   al. 2014). The HCLs in subduction zones and regional metamorphic belts might be

287   related to the dehydration of pelite.

13

288   Wannamaker et al. (2009) studied the fluid and deformation regime of an advancing

289   subduction system in Marlborough, New Zealand. The conductive zones were interpreted

290   to represent fluids that had migrated upward into the deep crust from source areas with

291   progressively higher metamorphic grades along the northwest-dipping subduction zone.

292   Two conductors that moderately correlate with the Hope and the Porters Pass fault zones

293   are suggested to correspond to the presence of aqueous fluid that formed during the

294   sediment dehydration (Wannamaker et al. 2009). However, there exist no laboratory data

295   that indicate the two HCLs were caused by the dehydration of sediments. We applied the

296   electrical conductivities of mudstone to establish a laboratory-based conductivity–depth

297   profile for the middle to lower crust of the advancing subduction system under

298   Marlborough, New Zealand. To that end, it was crucial to determine the temperature field

299   by converting the conductivity–temperature data into conductivity–depth data. The

300   relationship between temperature and depth in the Earth's stationary crust can be

301   described by a numerical solution of the heat conduction equation (Čermák and

302   Laštovičková 1987):

303
$$T = T_0 + (\frac{Q}{k})Z - (\frac{A_0}{2k})Z^2 \tag{4}$$

304   where T_0 is the surface temperature (K), Q is the surface heat flow (mW/m^2), Z is the

305   lithospheric layer depth (km), k is thermal conductivity (W/mK), and A_0 is the

306   lithospheric radiogenic heat productivity (μW/m^3). Based on previous studies, the thermal

307   calculation parameters for Marlborough are $Q = 70$ mW/m^2 (Wannamaker et al. 2009), A_0

308    $= 1.1$ μW/m^3, and $k = 2.5$ W/mK (Ranalli and Rybach 2005).

309   Based on previous MT results (Wannamaker et al. 2009), two conductivity–depth

310   profiles were constructed for HCLs that moderately correlate with the Hope and Porters

311   Pass fault zones in Marlborough, New Zealand (Fig. 7). Our laboratory-based

312   conductivity–depth profiles for mudstone were obtained at 623–973 K. Fig. 7 shows that

313   the electrical conductivities of the mudstone samples after dehydration were close to

314   those of HCL in the shallow crust in Marlborough, New Zealand. This result is consistent

315   with the conclusion of Wannamaker et al. (2009) that the two conductors are caused by

316   aqueous fluid ascending from source areas into the deep crust and that the fluid formed

317   by the dehydration of sediments. Therefore, the fluid formed by the dehydration of pelite

318   is confirmed to be an important factor causing HCLs in Marlborough, New Zealand.

319

320   **ACKNOWLEDGEMENTS**

332

15

REFERENCES CITED

333

334 Čermák, V., and Laštovičková, M. (1987) Temperature profiles in the earth of importance to deep

335   electrical conductivity models. Pure and Applied Geophysics, 25, 255-284.

336 Dai, L.D., and Karato, S. (2014a) High and highly anisotropic electrical conductivity of the

337   asthenosphere due to hydrogen diffusion in olivine. Earth and Planetary Science Letters, 408,

338   79-86.

339 Dai, L.D., and Karato, S. (2014b) Influence of FeO and H on the electrical conductivity of olivine.

340   Physics of the Earth and Planetary Interiors, 237, 73-79.

341 Dai, L.D., Hu, H.Y., Li, H.P., Jiang, J.J., and Hui, K.S. (2014) Influence of temperature, pressure, and

342   chemical composition on the electrical conductivity of granite. American Mineralogist, 99,

343   1420-1428.

344 Dai, L.D., Hu, H.Y., Li, H.P., Hui, K.S., Jiang, J.J., Li, J., and Sun, W.Q. (2015) Electrical

345   conductivity of gabbro: the effects of temperature, pressure and oxygen fugacity. European

346   Journal of Mineralogy, 27, 215-224.

347 Dai, L.D., Hu, H.Y., Li, H.P., Wu, L., Hui, K.S., Jiang, J.J., and Sun, W.Q. (2016) Influence of

348   temperature, pressure, and oxygen fugacity on the electrical conductivity of dry eclogite, and

349   geophysical implications. Geochemistry Geophysics Geosystems, 17, 2394-2407.

350 Dai, L.D., Li, H.P., Hu, H.Y., and Shan, S.M. (2008) Experimental study of grain boundary electrical

351   conductivities of dry synthetic peridotite under high-temperature, high-pressure, and different

352   oxygen fugacity conditions. Journal of Geophysical Research: Solid Earth, 113, B12211.

353 Fuji-ta, K., Katsura, T., Matsuzaki, T., Ichiki, M., and Kobayashi, T. (2007) Electrical conductivity

354   measurement of gneiss under mid- to lower crustal *P-T* conditions. Tectonophysics, 434, 93-101.

355   Fuji-ta, K., Katsura, T., and Tainosho, Y. (2004) Electrical conductivity measurement of granulite

356   under mid- to lower crustal pressure-temperature conditions. Geophysical Journal International,

357   157, 79-86.

358   Gaillard, F., Malki, M., Iacono-Marziano, G., Pichavant, M., and Scaillet, B. (2008) Carbonatite melts

359   and electrical conductivity in the asthenosphere. Science, 322, 1363-1365.

360   Gao, L.E., and Zeng, L.S. (2014) Fluxed melting of metapelite and the formation of Miocene

361   high-CaO two-mica granites in the Malashan gneiss dome, southern Tibet. Geochimica et

362   Cosmochimica Acta, 130, 136-155.

363   Gao, L.E., Zeng, L.S., Wang, L., Hou, K.J., Guo, C.L., and Tang, S.H. (2013) Age and formation

364   mechanism of the Malashan high-Ca two-mica granite within the Northern Himalayan Gneiss

365   Domes, southern Tibet. Acta Petrologica Sinica, 29, 1995-2012.

366   Guo, X.Z. (2016) Experimental study of the electrical conductivity of hydrous minerals in the crust

367   and the mantle under high pressure and high temperature. Science China-Earth Science, 59,

368   696-706.

369   Guo, X.Z., and Yoshino, T. (2014) Pressure-induced enhancement of proton conduction in brucite.

370   Geophysical Research Letters, 41, 813-819.

371   Guo, X.Z., Yoshino T., and Katayama I. (2011) Electrical conductivity anisotropy of deformed talc

372   rocks and serpentinites at 3 GPa. Physics of the Earth and Planetary Interiors, 188, 60-81.

373   Hawkesworth, C.J., Turner, S.P., McDermott, F., Peate, D.W., and van Calsteren P. (1997) U-Th

374   isotopes in arc magmas: Implications for element transfer from the subducted crust. Science, 276,

375   551-555.

376   Hu, H.Y., Dai, L.D., Li, H.P., Hui, K.S., and Sun, W.Q. (2017) Influence of dehydration on the

377   electrical conductivity of epidote and implications for high conductivity anomalies in subduction

378   zoens. Journal of Geophysical Research: Solid Earth, 122, 2751-2762.

379   Hu, H.Y., Li, H.P., Dai, L.D., Shan, S.M., and Zhu, C.M. (2013) Electrical conductivity of albite at

380   high temperatures and high pressures. American Mineralogist, 96, 1821-1827.

381   Hu, H.Y., Dai, L.D., Li, H.P., Jiang, J.J., and Hui, K.S. (2014) Electrical conductivity of K-feldspar at

382   high temperature and high pressure. Mineralogy and Petrology, 108, 609-618.

383   Hu, H.Y., Li, H.P., Dai, L.D., Li, H.P., Hui, K.S., and Li, J. (2015) Temperature and high pressure

384   dependence of electrical conductivity in synthetic anorthite. Solid State Ionics, 276, 136-141.

385   Huang, C.M., Zhao, Z.D., Zhu, D.C., Liu, D., Huang, Y., Dung, M.C., Hu, Z.C., and Zheng, J.P.

386   (2013) Geochemistry, zircon U-Pb chronology and Hf isotope of Luozha leucogranite, southern

387   Tibet. Acta Petrologica Sinica, 29, 3689-3702.

388   Huebner, J.S., and Dillenburg, R.G. (1995) Impedance spectra of hot, dry silicate minerals and

389   rock-qualitative interpretation of spectra. American Mineralogist, 80, 46-64.

390   Hyndman, R.D., Vanyan, L.L., and Marquis, G. (1993) The origin of electrically conductive lower

391   continental crust: saline water or graphite? Physics of the Earth and Planetary Interiors, 81,

392   325-344.

393   Li, Y., Tang, H.F., Liu, C.Q., and Hou, G.S. (2005) The high pressure differential thermal study of

394   dehydration effect of pelite. Acta Petrological Sinica 21, 986-992.

18

395   Li, Y., Yang, X.Z., Yu, J.H., and Cai, Y.F. (2016) Unusually high electrical conductivity of phlogopite:

396   the possible role of fluorine and geophysical implications. Contributions to Mineralogy and

397   Petrology, 171, 37.

398   Manthilake, G., Bolfan-Casanova, N., Novella, D., Mookherjee, M., and Andrault, D. (2016)

399   Dehydration of chlorite explains anomalously high electrical conductivity in the mantle wedges.

400   Science Advances, 2, e1501631.

401   Manthilake, G., Mookherjee, M., Bolfan-Casanova, N., and Andrault, D. (2015) Electrical

402   conductivity of lawsonite and dehydrating fluids at high pressures and temperatures. Geophysical

403   Research Letters, 42, 7398-7405.

404   Maumus, J., Bagdassarov, N., and Schmeling, H. (2005) Electrical conductivity and partial melting of

405   mafic rocks under pressure. Geochimica et Cosmochimica Acta, 69, 4703-4718.

406   Ni, H., Keppler, H., and Behrens, H. (2011) Electrical conductivity of hydrous basaltic melts:

407   implications for partial melting in the upper mantle. Contributions to Mineralogy and Petrology,

408   162, 637-650.

409   Ogawa, Y., Nishida, Y., and Makino, M. (1994) A collision boundary imaged by magnetotellurics,

410   Hidaka mountains, central Hokkaido, Japan. Journal of Geophysical Research: Solid Earth, 99,

411   22373-22388.

412   Podoba, R., Štubňa, I., Trnovcová, V., and Trník, A. (2014) Temperature dependence of DC electrical

413   conductivity of kaolin. Journal of Thermal Analysis and Calorimetry, 118, 597-601.

414   Ranalli, G. and Rybach L. (2005) Heat flow, heat transfer and lithosphere rheology in geothermal

415   areas: Features and examples. Journal of Volcanology and Geothermal Research, 148, 3-19.

416   Rao, C.K., Selvaraj, C., and Gokarn, S.G. (2014) Deep electrical structure over the igneous arc of the

417   Indo Burman Orogen in Sagaing province, Myanmar from magnetotelluric studies. Journal of

418   Asian Earth Sciences, 94, 68-76.

419   Roberts, J.J., and Tyburczy, J.A. (1991) Frequency dependent electrical properties of polycrystalline

420   olivine compacts. Journal of Geophysical Research: Solid Earth, 96, 16205-16222.

421   Robertson, K., Taylor, D., Thiel, S., and Heinson, G. (2015) Magnetotelluric evidence for

422   serpentinisation in a Cambrian subduction zone beneath the Delamerian Orogen, southeast

423   Australia. Gondwana Research, 28, 201-211.

424   Satoh, H., Nishida, Y., Utsugi, M., Hirano, K., Doi, T., and Arita, K. (1998) Resistivity structure in

425   and around the Southern Part of Hidaka Metamorphic Belt, Hokkaido, as inferred from

426   magnetotelluric investigations. Geophysical Bulletin of Hokkaido University, 61, 59-68.

427   Song, S.G., Niu, Y.L., Zhang, L.F., Wei, C.J., Liou, J.G., and Su, L. (2009) Tectonic evolution of

428   early Paleozoic HP metamorphic rocks in the North Qilian Mountains, NW China: New

429   perspectives. Journal of Asian Earth Sciences, 35, 334-353.

430   Song, S.G., Wang, M.Y., Wang, C., and Liu, Y.L. (2015) Magmatism and continental crust net growth

431   in the process of Continental orogenic belt collision-subduction-turnback-collapse. Science

432   China-Earth Sciences, 45, 916-940.

433   Song, M.S., Xie, H.S., Zheng, H.F., Guo, J., Xu, Y.S., and Xu, Z.M. (1996)

434   Determination of serpentine dehydration temperature at 1-5 GPa by the method of electrical

435   conductivity. Chinese Science Bulletin, 41, 1815-1819.

436   Tsuno, K., and Dasgupta, R. (2012) The effect of carbonates on near-solidus melting of pelite at

437   relative efficiency of H_2O and CO_2 subduction. Earth and Planetary Science Letters, 319-320,

438   185-196.

439   Walther, J.V., and Orville, P.M. (1982) Volatile production and transport in regional metamorphism.

440   Contributions to Mineralogy and Petrology, 79, 252-257.

441   Wannamaker, P.E., Caldwell, T.G., Jiracek, G.R., Maris, V., Hill, G.J., Ogawa, Y., Bibby, H.M.,

442   Bennie, S.L. and Heise, W. (2009) Fluid and deformation regime of an advancing subduction

443   system at Marlborough, New Zealand. Nature, 460, 733-736.

444   Wyllie, P.J. (1982) Subduction products according to experimental prediction. Geological Society of

445   America Bulletin, 93, 468-476.

446   Xie, H.S., Zhou, W.G., Zhu, M.X., and Liu, Y.G. (2002) Elastic and electrical properties of

447   serpentinite dehydration at high temperature and high pressure. Journal of Physics: Condensed

448   Matter, 14, 11359-11363.

449   Yakymchuk, C., and Brown, M. (2014) Consequences of open-system melting in tectonics. Journal of

450   the Geological Society, 171, 21-40.

451   Yang, X.Z. (2012) Orientation-related electrical conductivity of hydrous olivine, clinopyroxene and

452   plagioclase and implications for the structure of the lower continental crust and uppermost mantle.

453   Earth and Planetary Science Letters, 317-318, 241-250.

454   Yang, X.Z., Keppler, H., McCammon, C., Ni, H.W., Xia, Q.K., Fan, Q.C. (2011) Effect of water on

455   the electrical conductivity of lower crustal clinopyroxene. Journal of Geophysical Research:

456   Solid Earth, 116, B04208.

457   Yang, X.Z., and McCammon, C. (2012) Fe^{3+}-rich augite and high electrical conductivity in the deep

458   lithosphere. Geology, 40, 131-134.

459   Yoshino, T., Matsuzaki, T., Shatskiy, A., and Katsura, T. (2009) The effect of water on the electrical

460   conductivity of olivine aggregates and its implications for the electrical structure of the upper

461   mantle. Earth and Planetary Science Letters, 288, 291-300.

462   You, C.F., Castillo, P.R., Gieskes, J.M., Chan, L.H., and Spivack, A.J. (1996) Trace element behavior

463   in hydrothermal experiment: Implications for fluid processes at shallow depths in subduction

464   zones. Earth and Planetary Science Letters, 140, 41-52.

465   Zhu, M.X., Xie, H.S., Guo, J., Bai, W.M., and Xu, Z.M. (2001) Impedance spectroscopy analysis on

466   electrical properties of serpentine at high pressure and high temperature. Science China-Earth

467   Science, 44, 336-345.

468   Zhu, M.X., Xie, H.S., Guo, J., Zhang, Y.M., and Xu, Z.M. (1999) Electrical conductivity

469   measurement of serpentine at high temperature and pressure. Chinese Science Bulletin, 44,

470   1903-1907.

22

471   **Figure captions**

472   **Fig. 1** Sample assembly for electrical conductivity measurements at high temperatures

473   and pressures.

474   **Fig. 2** Representative complex impedance spectra of the mudstone samples at 2.5 GPa

475   and 623–973 K.

476   **Fig. 3** Logarithm of the electrical conductivities versus the reciprocal temperatures of the

477   samples at 0.5–2.5 GPa and 623–973 K.

478   **Fig. 4** Logarithm of the electrical conductivities versus the reciprocal temperatures of the

479   samples during different heating/cooling cycles at 1.5 GPa.

480   **Fig. 5** Relationship between the electrical conductivities of the mudstone sample and

481   time at 2.5 GPa and 823 K.

482   **Fig. 6** Comparison of the electrical conductivities of the mudstone samples measured at

483   0.5–2.5 GPa in this study and in previous studies. The dashed purple and blue lines

484   represent the electrical conductivities of serpentine and talc at 3.0 GPa from Zhu et

485   al. (1999) and Guo et al. (2011), respectively, the dashed brown line represents the

486   electrical conductivity of granulite at 1.0 GPa from Fuji-ta et al. (2004), the dashed

487   green line represents the electrical conductivity of lawsonite before and after

488   dehydration at 7.0 GPa from Manthilake et al. (2015), and the dashed red line

489   represents the electrical conductivity of phlogopite at 1.0 GPa from Li et al. (2016).

490   **Fig. 7** Laboratory-based conductivity–depth profiles constructed from data of the

491   mudstone samples before and after dehydration, and the thermodynamic parameters,

23

492   and comparison with geophysically inferred field results from Marlborough, New

493   Zealand. The black solid lines represent the conductivity–depth profiles based on

494   the conductivities of the samples described in Fig. 3 and based on a surface heat

495   flow of 70 mW/m^2 in Marlborough. The red and blue dashed lines represent the

496   magnetotelluric data derived from two high-conductivity layers that are moderately

497   correlated with the Hope and Porters Pass fault zones in Marlborough (Wannamaker

498   et al. 2009), respectively.

24

Table 1 Fitting parameters for electrical conductivity of mudstone before and after dehydration.

Run no.	P (GPa)	T (K)	Log σ_0 (S/m)	ΔH (eV)	R^2	ΔU (eV)	ΔV (cm^3/mol)
DS6	0.5	623−773	1.45±0.03	0.75±0.03	0.9998	0.78±0.01	-0.06±0.01
		873−973	0.92±0.16	0.59±0.01	0.9950	0.65±0.02	-0.12±0.01
DS7	1.5	623−773	1.80±0.16	0.70±0.03	0.9971	0.78±0.01	-0.06±0.01
		823−973	1.18±0.12	0.49±0.02	0.9952	0.65±0.02	-0.12±0.01
DS8	2.5	623−723	1.40±0.20	0.64±0.05	0.9998	0.78±0.01	-0.06±0.01
		823−973	0.94±0.07	0.36±0.03	0.9950	0.65±0.02	-0.12±0.01

Table 2 Mineralogical assemblage of mudstone and dehydration products. Ms=muscovite, Kln=kaolinite, Metakln= metakaolinite, Qz=quartz, Hem=hematite and Mgh=maghemite.

	P (GPa)	T (°C)	No.	Mineral associations
Before dehydration	/	/	DS5	Kln (40%) + Ms (30%) + Qz (20%) + Hem (5%) + Mgh (5%)
After dehydration	0.5	530–700	DS6	Metakln (40%) + Ms (30%) + Qz (20) + Hem (5%) + Mgh (5%)
	1.5	500–700	DS7	Metakln (40%) + Ms (30%) + Qz (20) + Hem (5%) + Mgh (5%)
	2.5	490–700	DS8	Metakln (40%) + Ms (30%) + Qz (20) + Hem (5%) + Mgh (5%)

Figure 1

TC

1260FPIA
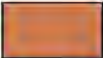
Pyrophyllite   stainless steel heater   Al$_2$O$_3$ Nickel foil   MgO

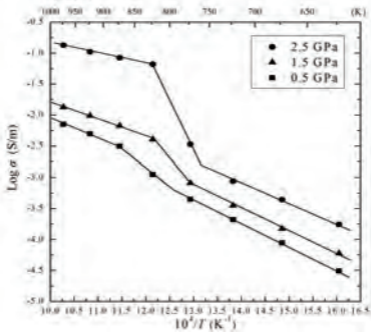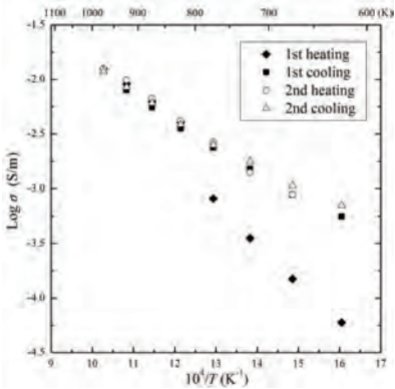Sample   Nickel electrode   Thermocouple   Lead wire   Ground wire

Figure 2
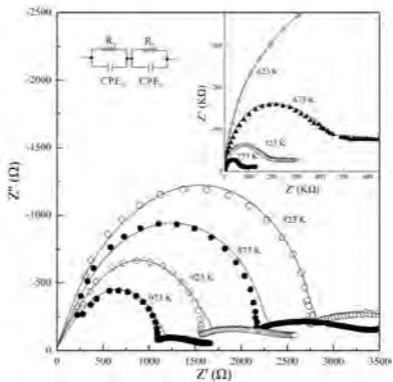
Figure 3

Figure 4

Figure 5
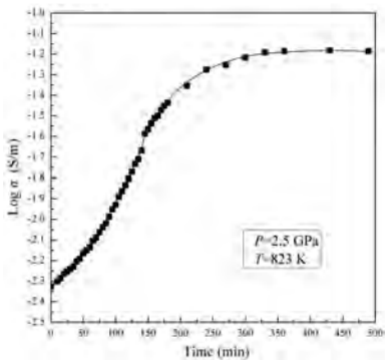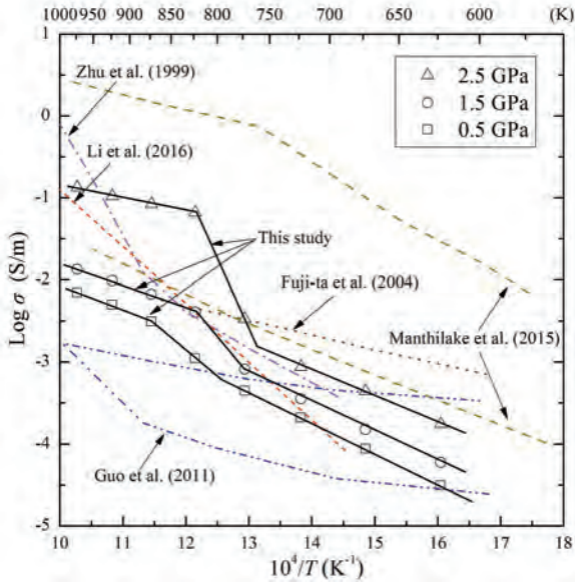
Figure 6

Figure 7